Intense Circular Dichroism and Spin Selectivity in $AgBiS_2$ Nanocrystals by Chiral Ligand Exchange

Ding, Pengbo; Chen, Dezhang; Tamtaji, Mohsen; Hu, Sile; Qammar, Memoona; Ko, Pui Kei; Sergeev, Aleksandr A.; Zou, Bosen; Tang, Bing; Wong, Kam Sing; Guo, Liang; Chen, Guanhua; Rogach, Andrey L.; Halpert, Jonathan E.

Published in:
Advanced Materials

Published: 27/12/2024

Document Version:
Final Published version, also known as Publisher's PDF, Publisher's Final version or Version of Record

Published version (DOI):
10.1002/adma.202410087

Publication details:
Ding, P., Chen, D., Tamtaji, M., Hu, S., Qammar, M., Ko, P. K., Sergeev, A. A., Zou, B., Tang, B., Wong, K. S., Guo, L., Chen, G., Rogach, A. L., & Halpert, J. E. (2024). Intense Circular Dichroism and Spin Selectivity in $AgBiS_2$ Nanocrystals by Chiral Ligand Exchange. *Advanced Materials*, *36*(52), Article 2410087. https://doi.org/10.1002/adma.202410087

ADVANCED MATERIALS
www.advmat.de

Intense Circular Dichroism and Spin Selectivity in $AgBiS_2$ Nanocrystals by Chiral Ligand Exchange

Pengbo Ding, Dezhang Chen, Mohsen Tamtaji, Sile Hu, Memoona Qammar, Pui Kei Ko, Aleksandr A. Sergeev, Bosen Zou, Bing Tang, Kam Sing Wong, Liang Guo, Guanhua Chen,* Andrey L. Rogach,* and Jonathan E. Halpert**

Chiral semiconducting nanomaterials offer many potential applications in photodetection, light emission, quantum information, and so on. However, it is difficult to achieve a strong circular dichroism (CD) signal in semiconducting nanocrystals (NCs) due to the complexity of chiral ligand surface engineering and multiple, uncertain mechanisms of chiroptical behavior. Here, a chiral ligand exchange strategy with cysteine on the ternary metal chalcogenide $AgBiS_2$ NCs is developed, and a strong, long-lasting CD signal in the near-UV region is achieved. By carefully optimizing the ligand concentration, the CD peaks are observed at 260 and 320 nm, respectively, giving insight into the different ligand binding mechanisms influencing the CD signal of $AgBiS_2$ NCs. Using density-functional theory, a large degree of crystal distortion by the bidentate mode of ligand chelation, and efficient ligand-NC electron transfer, synergistically resulting in the strongest CD signal (g-factor over 10^{-2}) observed in chiral ligand-exchanged semiconductor NCs to date, is demonstrated. To demonstrate the effective chiral properties of these $AgBiS_2$ NCs, a spin-filter device with over 86% efficiency is fabricated. This work represents a considerable leap in the field of chiral semiconductor NCs and points toward their future applications.

1. Introduction

Chiral nanocrystals (NCs) exhibit unique chiroptical characteristics, offering substantial promise for a wide range of applications, such as circularly polarized photodetectors,[1] spin-based light-emitting diodes,[2] advanced bioimaging techniques,[3] quantum computing,[4] and spintronics.[5] Essentially, there exist three methods to imbue NCs with chirality: i) incorporating chiral ligands upon the surface of NCs,[6] ii) adopting a chiral shape or chiral shell on NCs surface,[7] and iii) fabricating chiral assemblies created by arranging NCs within a chiral matrix.[8] In contrast to achieving self-assembled chiral shapes or assemblies which necessitate stringent reaction conditions,[7a,8] the direct attachment of chiral ligands is the most straightforward and attainable approach conducted through the ligand exchange technique. To date, numerous conventional NCs exchanged by chiral ligands have been shown to exhibit chirality, including perovskite[9] and metal chalcogenide NCs,[10] and carbon dots.[11] However, compared with plasmonic gold nanoparticles[7a] or 2D perovskites,[12] conventional semiconductor NCs could only achieve relatively low absorption dissymmetry factors so far, ranging from 10^{-5} to 10^{-3}.[6b,10,13] Despite the considerable gap in chirality between NCs and other chiral materials, the NCs'

P. Ding, D. Chen, M. Qammar, P. K. Ko, B. Zou, J. E. Halpert
Department of Chemistry
The Hong Kong University of Science and Technology
Hong Kong SAR 999077, China
E-mail: jhalpert@ust.hk

P. Ding, L. Guo
Department of Mechanical and Energy Engineering
Southern University of Science and Technology
Shenzhen 518055, China
E-mail: guol3@sustech.edu.cn

M. Tamtaji, G. Chen
Hong Kong Quantum AI Lab Limited
Pak Shek Kok, Hong Kong SAR 999077, China
E-mail: ghc@everest.hku.hk

S. Hu, B. Tang, A. L. Rogach
Department of Materials Science and Engineering
and Centre for Functional Photonics (CFP)
City University of Hong Kong
Hong Kong SAR 999077, China
E-mail: andrey.rogach@cityu.edu.hk

A. A. Sergeev, K. S. Wong
Department of Physics
The Hong Kong University of Science and Technology
Hong Kong, Hong Kong SAR 999077, China

L. Guo
SUSTech Energy Institute for Carbon Neutrality
Southern University of Science and Technology
518055 Shenzhen, China

G. Chen
Department of Chemistry
The University of Hong Kong
Hong Kong SAR 999077, China

The ORCID identification number(s) for the author(s) of this article can be found under https://doi.org/10.1002/adma.202410087

DOI: 10.1002/adma.202410087

remarkable optical properties, exceptional stability, and straightforward synthesis methods present a novel opportunity for advancing chiral material development.

Chiroptical behavior in dispersed NCs has been generally ascribed to either crystal lattice distortions in the NC surface, caused by the chiral ligands,[6a] or to electronic interactions between the ligands and the NCs.[6b] Both conditions are difficult to achieve and depend on specific nanomaterial properties. For lattice distortion, in metals and binary semiconductors, the crystal lattice tends to be highly ordered and rigid such that the surface ligands have minimal effect on the overall crystal structure. In the case of perovskite NCs, their fragility prevents complete ligand exchange, resulting in a mixed ligand surface that diminishes chiroptical behavior.[9,14] Regarding electronic interactions, ligands can imprint their chirality onto the electronic structure of NCs or establish orbital hybridization between ligands and NCs,[6b,15] necessitating specific nanomaterials with appropriate band structures. Alternatively, ternary or quaternary chalcogenide systems may provide a superior avenue for introducing chirality. Cation disorder, the deviation of atomic positions in the cationic sublattice, is found to be common in ternary metal chalcogenides.[16] This disordered cation sublattice can increase the distorting effects of the surface chiral ligands. The surface disorder can also aid in carrier localization to the surface,[17] where charge extraction then becomes easier with the right choice of ligands.

Here, we have conducted the direct ligand exchange to introduce the chiral ligand cysteine on the ternary metal chalcogenide $AgBiS_2$ NCs, which are nontoxic and have recently emerged as a strongly absorbing nanocrystalline material for solar cells and photodetectors.[18,37] The resulting chiral NCs exhibit an unprecedented strong CD signal at near UV range with a *g*-factor $\approx 1 \times 10^{-2}$, which is one of the highest among all the semiconducting chiral NCs.[6b,10,13] By adjusting the ligand concentration to switch from mono- to bidentate binding modes, we are able to show that both crystal distortion and electron transfer play roles in creating the strong CD signals of this material. As a demonstration, we have also fabricated the first $AgBiS_2$ spintronic device to filter the in-phase electrons and used magnetic conductive probe atomic force microscopy (mCP-AFM) to measure the spin polarization (SP) efficiency, achieving an SP efficiency of over 86%. This represents a new record for chalcogenide NC spin filters. Our work suggests that applying chiral ligand exchange on ternary metal chalcogenides would exert strong lattice distortion and charge transfer simultaneously, which significantly improves the chiroptical properties of the nontoxic NCs for a variety of future applications.

2. Results and Discussion

2.1. Chirality Induction Through Chiral Ligand Exchange

We have developed a direct solution-phase ligand exchange for obtaining high-quality, stable cysteine-capped $AgBiS_2$ NCs (Experimental Section). The pristine oleic acid (OA)-capped $AgBiS_2$ NCs in toluene were added to a solution of L-/D-cysteine in water (**Figure 1a**). Additional tetramethylammonium hydroxide (TMAH) was added to deprotonate the sulfur in cysteine and facilitate the exchange process. After vigorous stirring and setting, $AgBiS_2$ NCs were transferred from the top toluene phase to the bottom aqueous phase (Figure 1b). UV–vis spectra show negligible differences after the exchange process, indicating that the exchange process does not significantly affect the static optical properties of the NC cores (Figure 1c). The absorbance peaks from 250 to 300 nm for the OA-NCs are assigned to absorption by the oleate ligand and these peaks are observed to disappear after the ligand exchange (Figure S1, Supporting Information) The Fourier-transform infrared (FTIR) spectroscopy also shows that the C—H stretch signal at 3000 cm^{-1} has been greatly suppressed after the ligand exchange, indicating that the long OA ligands were replaced by the shorter cysteine ligands during the process (Figure 1d). We performed the CD measurements on the Cys-NCs and obtained two strong, mirrored CD signals on the L-Cys-NC and D-Cys-NC samples, respectively (Figure 1e). The CD spectra have two peaks at 260 and 320 nm. This is very different from CD spectra of pure L-/D-cysteine (Figure 1e, dashed lines), which shows some features only at deeper UV wavelengths (<250 nm), indicating that the strong CD signal from the Cys-NC hybrid does not result from cysteine alone, but from the Cys-NCs. Additionally, we measured the CD signal of the supernatants from two purification steps to exclude the contribution of metal complexes to the chiral signals (Figure S2, Supporting Information). We notice that this chiral ligand exchange approach can be extended to analogous chiral ligands, such as penicillamine (Figure S3, Supporting Information).

We have further optimized the ligand exchange parameters by finely tuning the reactant concentration. By adjusting the concentration of cysteine and TMAH (additional data are presented in Tables S1 and S2, Supporting Information), the g-factors of CD signal (g_{CD}) at 260 and 320 nm peaks were measured and a matrix was constructed to illustrate the observed effects, as shown in **Figure 2a,b**. As TMAH provides basicity and suitable pH to deprotonate thiol group on cysteine, the correct ratio of TMAH to cysteine is critical for obtaining a high CD signal. The relative peaks of the CD signal at 320 and 260 nm are located in the corners of the representative matrices, at the 0.02 and 0.3 M concentrations of cysteine, respectively. $AgBiS_2$ NC samples that have been ligand-exchanged under those conditions are labeled as Cys(0.02 M)-NC and Cys(0.3 M)-NC. Figure 2c,d shows the corresponding g-factor CD graph, with peaks at 260 and 320 nm. The g-factor of CD (g_{CD}) values was calculated according to the following equation:[9]

$$g_{CD} = \frac{A_L - A_R}{A} = \frac{CD[\text{mdeg}]}{32980A} \quad (1)$$

where A_L and A_R represent left and right circularly polarized light absorbance, A is linear polarized light absorbance, and CD is the corresponding CD peak intensity in millidegree (mdeg). By gradually increasing the concentration of cysteine, the peak CD at 320 nm decreased slightly. With a gradual increase in cysteine concentration, the peak CD at 320 nm tends to decrease, being in line with the previous reports on cysteine-capped CdSe-CdS QDs' CD signals.[13a] At the same time, the 260-nm peak shows an opposite trend with a gradual rise up to 9.8×10^{-3} at a cysteine concentration of 0.3 M and saturation after that. To the best of our knowledge, the g-factor here is one of the highest values reported for any of the chiral NCs (Figure 2e; Table S3,

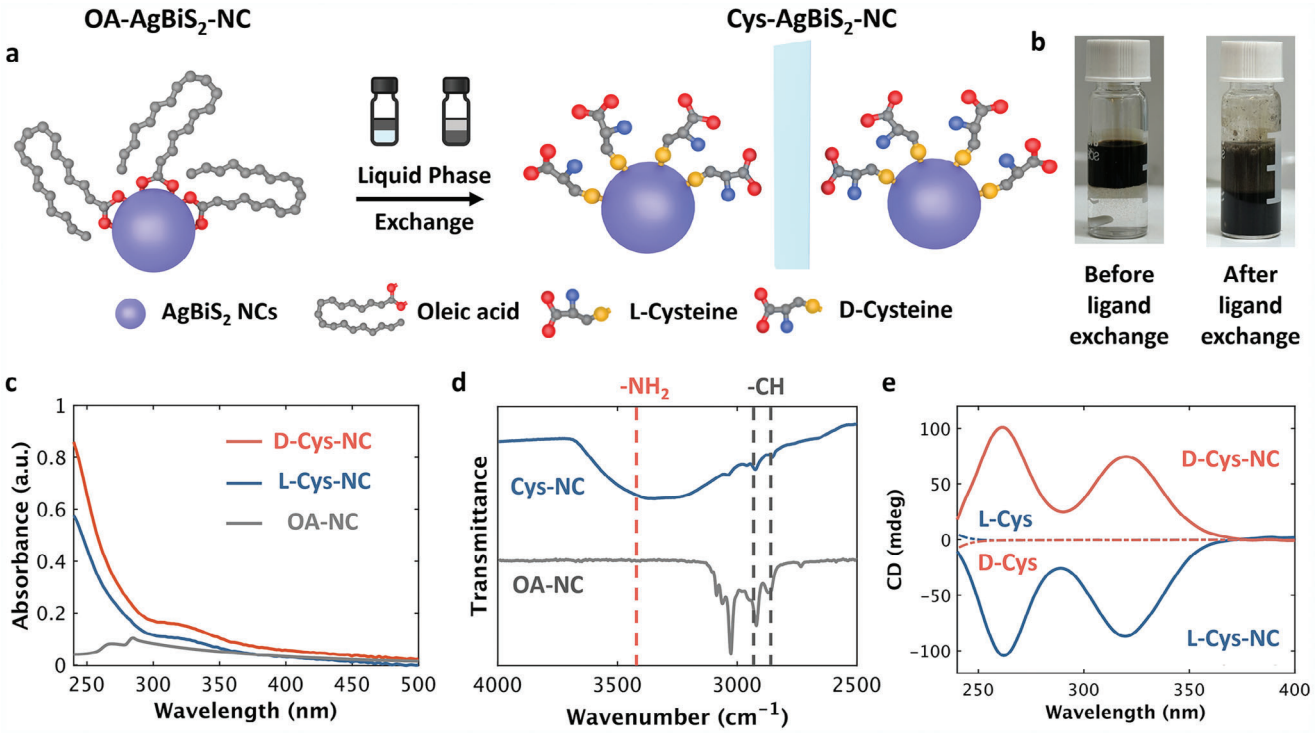

Figure 1. a) Schematic of solution-phase ligand exchange with a chiral ligand cysteine performed on $AgBiS_2$ NCs. b) Photographs of the solution phase indicating the successful transfer of $AgBiS_2$ NCs from toluene to water. c) UV–vis spectra and d) FTIR spectra of $AgBiS_2$ NCs before and after the chiral ligand exchange. Dashed lines in d) represent —NH_2 and —CH bonds. e) CD spectra of $AgBiS_2$ NCs exchanged with L-cysteine and D-cysteine, respectively. Dashed lines refer to the CD signal of pure L/D-cysteine in water.

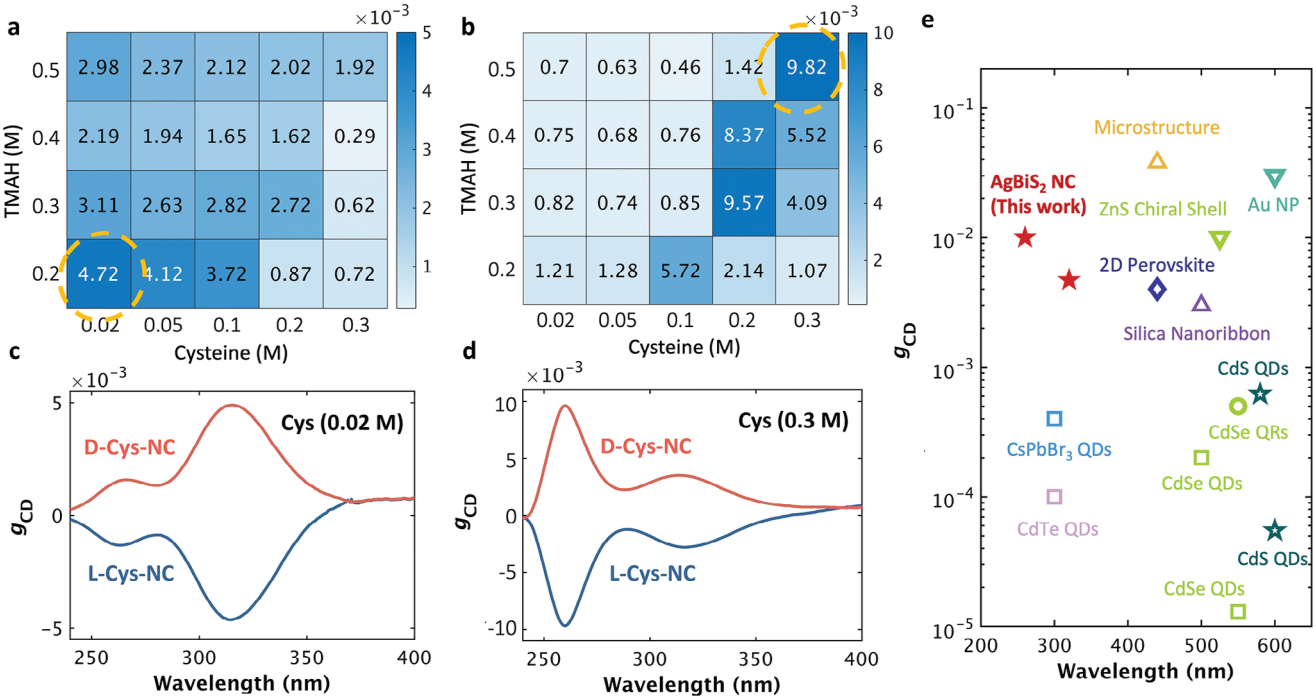

Figure 2. Matrices showing Cys-NC g-factors at a) 320 and b) 260 nm under different cysteine and TMAH concentrations used to synthesize the Cys-NC hybrids. The peak g-factor at 320 and 260 nm correspond to 0.02 and 0.3 M concentrations of cysteine. c) Wavelength-dependent g-factor of CD signal of Cys (0.02 M)-NC. d) Wavelength-dependent g-factor of CD signal of Cys (0.3 M)-NC. e) Comparison of the g-factor achieved in this study with other reported chiral nanomaterials (QD stays for quantum dots). See Table S1 (Supporting Information) for more details.[6–8,10,13,19]

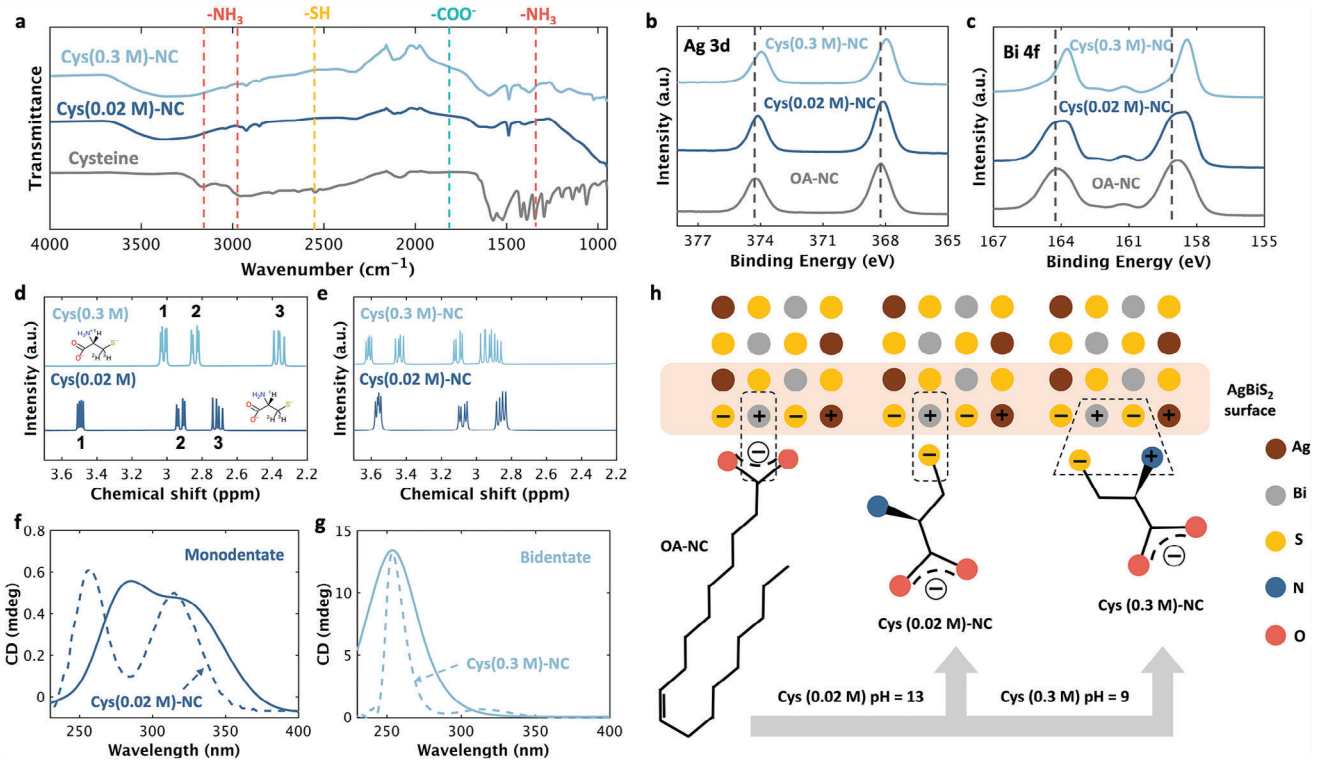

Figure 3. a) FTIR spectra of OA-NCs, Cys (0.02 M)-NCs, and Cys (0.3 M)-NCs. XPS spectra of b) Ag 3d and c) Bi 4f orbital of pristine and ligand-exchanged NCs, respectively. 1-H NMR spectra for d) cysteine exchanged solutions and e) Cys-NC hybrid. Simulated by TD-DFT CD signal of f) monodentate and g) bidentate binding modes for cysteine on the surface of $AgBiS_2$ NCs. Dashed lines represent the experimental CD signals of Cys (0.02 M)-NCs and Cys (0.3 M)-NCs. h) Schematics of major binding structures of OA-NCs, Cys (0.02 M)-NCs, and Cys (0.3 M)-NCs samples.

Supporting Information).[6–8,10,13,19] In addition, the Cys-NC samples in solution show high stability under ambient conditions (air, light, and humidity), retaining 70% intensity of the maximum recorded CD signal after 14 days (Figure S4, Supporting Information).

2.2. Nanocrystal-Ligand Binding Analysis

To better understand the origin of the varying CD peak intensities, we further investigated the binding structures of ligand exchanged-NCs. Although cysteine has been previously used to modify other metal chalcogenides,[13a,19b] it has not been applied to $AgBiS_2$ NCs and thus a thorough analysis is required. FTIR spectra in **Figure 3**a show that pure cysteine has a free ammonium (NH_3^+) stretch mode at 3125 cm^{-1}, which is significantly broadened after the ligand exchange, due to the binding of the ammonium group with the NC surface. The S—H stretch mode at 2552 cm^{-1} is completely diminished in the ligand exchanged-NCs, indicating that the sulfur has been fully deprotonated on the surface. The absence of a COO^- stretch ≈1730 cm^{-1} indicates that no binding occurs between the cysteine's carboxylate group and the NCs.[13a,20] Taken together, these phenomena suggest that cysteine is capable of binding to the $AgBiS_2$ NCs surface through its two terminal groups: i) a protonated ammonium group and ii) the deprotonated thiol group. We then used XPS to examine the state of the metal ions on the NC surface (Figure 3b,c). A downshift in the binding energy (E_B) is apparent for the Cys (0.02 M)-NCs Ag 3d orbital, indicating nearly complete removal of higher E_B Ag oleate. A further downshift is observed in Cys (0.3 M)-NCs indicating the complete removal of the oleate species. For the Bi 4f orbital, the evidence of oleate ligand removal is even more pronounced (Figure 3c). On the Cys (0.02 M)-NCs surface, Bi atoms have two E_B peaks, one due to Bi-oleate and another due to Bi-cysteine. In Cys (0.3 M)-NCs, again all the oleates appear to have been replaced by cysteine. This suggests that the binding structures of Cys (0.02 M)-NCs and Cys (0.3 M)-NCs are different, with the oleate species in the Cys (0.02 M)-NC samples only partially removed.

As a zwitterionic molecule, protonation of the functional groups on cysteine, and thus its binding activity, should depend on the pH of the solution. Therefore, we used proton nuclear magnetic resonance (1H-NMR) to visualize the surrounding chemical environment in the NC solution. Figure 3d presents the peaks in the pure cysteine exchange solution (0.02 and 0.3 M cysteine / TMAH blend without NCs). The α-H and β-H on the cysteine (^1H and $^{2/3}H$, respectively) show upfield shifting from 0.02 to 0.3 M samples due to the protonation of the NH_2 group. These results agree with the pH values of the Cys (0.02 M)-NC and Cys (0.3 M)-NC solutions, which were found to be 13 and 9, respectively. The pKa reference values of cysteine (pKa 1.8 for the carboxylate group, pKa ≈8.2 for the thiol group, pKa ≈10.3 for the ammonium group) suggest that the NH_3^+ groups should become deprotonated only in Cys (0.02 M) sample, where in

either case the thiol group is deprotonated.[21] Varying the cysteine/TMAH concentration forms different types of cysteine ions in the exchange solution, and therefore results in different ligand exchange mechanisms. Figure 3e shows the cysteine 1-H NMR peaks after the ligand exchange, and for both samples, the cysteine H peaks are shifted downfield. This occurs naturally when the ligands bind to the nanoparticles, resulting in a positively charged surface that facilitates electron transfer.[22] We also notice that in the Cys (0.3 M)-NC sample 6 quadruplets are observed, which indicates that cysteine binds to the surface with both monodentate and bidentate binding modes. The deprotonated thiol group binds with surface metal ions at either pH condition, while the ammonium group is only capable of binding to the surface in the Cys (0.3 M)-NC solution.

We then used time-dependent density-functional theory (TD-DFT) to further analyze the impact of the distinct binding modes on the CD peaks (see Experimental Section for details). From these calculations, the CD signal of the monodentate binding mode exhibited two peaks, situated at 280 and 330 nm (Figure 3f), respectively, which align with the experimental CD results of Cys (0.02 M)-NCs (minor peak shifts may be attributed to the presence of some OA ligands). In the bidentate binding mode, a remarkably strong CD peak at 260 nm is observed (Figure 3g), consistent with the experimental CD findings of Cys (0.3 M)-NCs. By reconciling the experimental findings with theoretical results, we ascertain that the bidentate binding mode within Cys (0.3 M)-NCs amplifies the signal dramatically (Figure S5, Supporting Information) higher than Cys (0.02 M)-NCs. Hence, TD-DFT provides evidence for the variations in CD peak positions and intensities caused by the different binding modes, corroborating the experimental results.

Based on the above results, we have provided a schematic of the binding structures of Cys-NCs under different ligand exchange conditions (Figure 3h). In the pristine OA-NCs, oleate ligands bind with the exposed positively charged metal ions as X-type ligands. In the Cys (0.02 M)-NC samples, cysteine ligands are fully deprotonated under high pH conditions, and the deprotonated neutral NH_2 can barely bind to the NC surface. As a result, cysteine binds to the NC surface in a monodentate arrangement via a sulfur-bismuth covalent bond. In Cys (0.3 M)-NCs, cysteine ligands provide an excess of protonated ammonium groups to bind to the surface sulfur (S from the $AgBiS_2$ lattice), resulting in a bidentate binding structure (S–Bi, NH_3^+-S). We expect that the bidentate binding results in a better-passivated surface and exerts a stronger crystal distortion effect; these explain the large increase in the apparent g_{CD} which will be further examined in the following DFT and XRD analysis.

2.3. Origin of Chirality in $AgBiS_2$

Three possible factors have been suggested to contribute to the appearance of CD in ligand-NC systems: i) chiral nanostructures, ii) lattice distortion, and iii) ligand-NC electron transfer.[6a] Although we did observe some aggregation after the ligand exchange due to the decreased molecular chain length and increased intermolecular attraction in Cys-NCs (Figures S6 and S7, Supporting Information), high-resolution transmission electron microscopy (HRTEM) confirmed that the morphology and dimensions of the NCs remain unchanged, and no chiral self-assembled nanostructures have developed.[23] Moreover, the near-linear increase in both the CD intensity and the absorbance negates the possibility of aggregation serving as the source of chiroptical properties (Figure S8, Supporting Information).[13b] Moreover, we conducted DFT calculations to analyze the contribution of the other two factors. As shown in **Figure 4a**, the lattice disorder in the Cys-NC samples increased by ≈14.5 and 20.5 $Da^{1/2}$ Å, respectively, as compared to the pristine OA-NCs (Tables S4 and S5, Supporting Information). This confirms that the bidentate ligand binding indeed exerts a strong distortion on the $AgBiS_2$ surface, which can contribute to the unusually strong g-factor observed. We further assessed the actual crystal distortion of the Cys-NC hybrid by XRD (Figure 4b) and found that the crystal distortion increased to 0.97% in Cys (0.02 M)-NCs and 1.32% in Cys (0.03 M)-NCs, respectively (Figure 4c; Figure S9, Supporting Information), as compared to that of the OA-NCs (0%). The lattice distortion we observed here is significantly higher than that of any other chiral nanomaterials, including perovskites (0.20%) and PbS (0.30%).[6a,24] We attribute this phenomenon to the disordered surface cations and softer sublattice in ternary metal chalcogenides,[16] which both contribute to strong CD signals.

In addition to stronger lattice distortion, the DFT studies suggest that electron transfer between cysteine ligand and $AgBiS_2$ NCs can also increase the CD signal of the Cys-NC hybrid. Figure 4d shows the theoretical Mulliken charge transfers of 0.31 and 0.86 e^- from $AgBiS_2$ NCs to cysteine for monodentate and bidentate binding modes, respectively, which strongly suggests that efficient charge transfer will occur. For monodentate binding mode, the charge transfer occurs between the S atom of cysteine and the Bi atom of $AgBiS_2$, where the 3p orbital of S hybridizes with the 6p orbital of the Bi atom. For bidentate binding mode, the charge transfer occurs between the S and N atoms of cysteine and Bi atoms of $AgBiS_2$, where the 3p orbital of S and 2p orbital of N hybridize with the 6p orbital of the Bi atoms. Transient absorption (TA) spectroscopy was then used to experimentally confirm the electron transfer. From the TA spectra of pristine OA-NC (Figure S10a, Supporting Information), we observe a positive $\Delta T/T$ signal ≈1050 nm matching well with the experimentally determined bandgap using Tauc's plots (Figure S11a, Supporting Information) and, therefore, attributed to the ground-state bleaching (GSB). For Cys-NCs, the GSB signal is less pronounced due to its superimposion with a strong sub-bandgap photoinduced absorption band (PIA), originating from carrier's excitation to higher energy states, self-trapping or absorption related to defect states. The last one is the most probable reason in our case due to surface defects inevitably appearing after ligand exchange. Moreover, after ligand exchange, the lattice distortion will change the bandgap due to the deformation potential effect.[25] As a result, the GSB position is shifted to 1050–1150 nm range (Figure S10b,c, Supporting Information), being well-consistent with Tauc plots (Figure S11b,c, Supporting Information). TA kinetics probed at the GSB range (Figure 4e) demonstrate a shorter decay time for Cys-NCs than OA-NCs, indicating the presence of electron transfer between $AgBiS_2$ NCs and cysteine. Together with sub-bandgap PIA, a new strong PIA

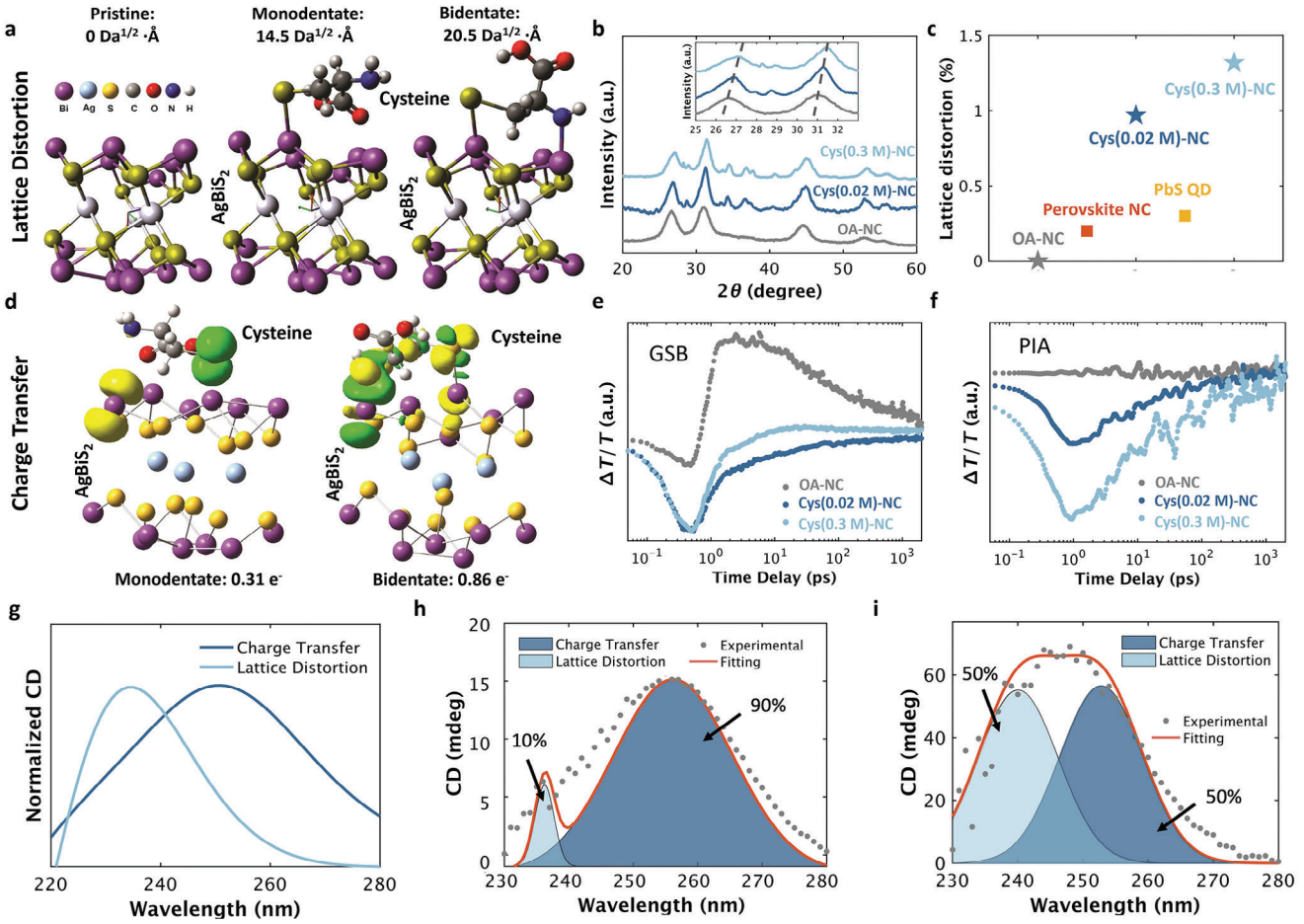

Figure 4. a) The side view of a fragment of $AgBiS_2$ lattice (left), and cysteine attached to the $AgBiS_2$ lattice through monodentate (middle) and bidentate (right) binding modes. b) Powder XRD of OA-NCs, Cys(0.02 M)-NCs, and Cys(0.3 M)-NCs; inset is a zoomed-in XRD result. c) Lattice distortion percentage of Cys(0.02 M)-NCs, and Cys(0.3 M)-NCs, and other referenced NCs. d) The side view of the Mulliken charge transfer from $AgBiS_2$ to cysteine with the isosurface of 0.005 $eÅ^{-3}$ in the case of monodentate (left) and bidentate (right) binding modes. Yellow and green colors represent the forward and reversed charge transfer, respectively. Transient absorption dynamics of e) GSB (probed at 1000–1100 nm for OA-NCs, and 1050–1150 nm for Cys-NCs) and f) PIA (probed at 600–800 nm) confirming the charge transfer between NCs and cysteine. g) TD-DFT simulated CD signals of lattice distortion and charge transfer by TD-DFT. The contribution of lattice distortion and charge transfer in h) Cys(0.02 M)-NCs, and i) Cys(0.3 M)-NCs, fitted from the TD-DFT data.

band appears in the 600–800 nm range after ligand exchange, which also demonstrates the charge transfer to a certain extent (Figure 4f).

To quantitatively assess the respective contributions of lattice distortion and charge transfer to the CD signal, we have calculated the individual contributions of these two mechanisms to the CD signal in the bidentate binding mode by TD-DFT. As depicted in Figure 4g, the two mechanisms contribute to the CD signal at distinct wavelengths, with lattice distortion's CD peak at 235 nm and charge transfer's CD peak at 255 nm. We have also observed that increasing the cysteine concentration caused the experimental CD peak of 260 to shift to 245 nm (Figure S12, Supporting Information), aligning with the TD-DFT findings. Hence, by fitting the experimental CD signal with the TD-DFT results, we can ascertain the proportional contributions to the CD signals from lattice distortion and charge transfer. For Cys (0.02 M)-NCs (Figure 4h), charge transfer contributes the majority of the CD signal. However, for Cys (0.3 M)-NCs (Figure 4i), the contribution of lattice distortion significantly intensifies, becoming nearly equivalent to that of charge transfer, culminating in the blue shift of the experimental CD signal. Thus, in contrast to previous studies,[6] this work demonstrates that lattice distortion and charge transfer jointly contribute to the highest CD signal (g_{CD} up to 1×10^{-2}) of Cys-$AgBiS_2$ NC hybrids yet observed for NCs in solution.

2.4. Spin Filter Based on Chiral $AgBiS_2$ Nanocrystals

Spin-dependent charge transport properties of Cys-NCs were investigated by magnetic conductive probe atomic force microscopy (mCP-AFM) with a Co-Cr-coated magnetic tip. This well-established method enables the assessment of spin filtering capabilities of chiral materials.[12b,27] The films were fabricated by drop-casting a solution of Cys (0.3 M)-NCs, as this concentration yielded higher quality thin films compared to those made with

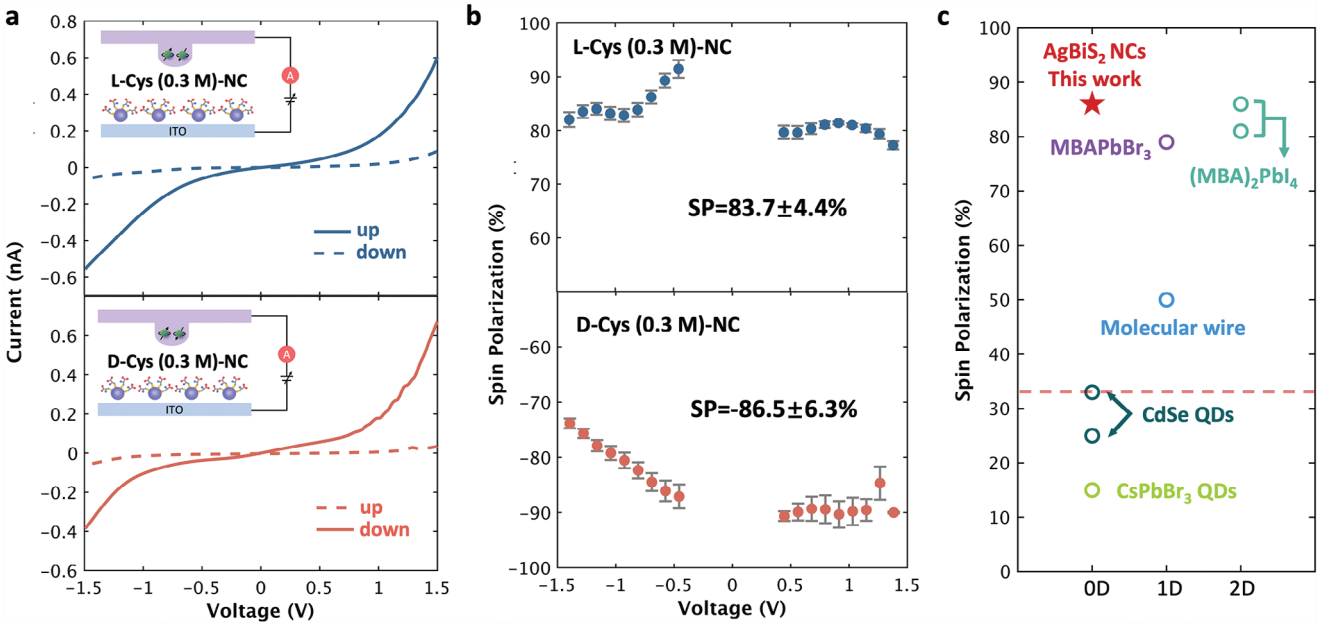

Figure 5. a) *I*–s*V* curves for L-Cys (0.3 M)-NC (top) and D-Cys (0.3 M)-NC (bottom) incorporated into spin filters are shown in the insets. b) Spin polarization of L-Cys (0.3 M)-NCs (top) and D-Cys (0.3 M)-NCs (bottom). c) Performance comparison with previously reported spin filters, with the dashed line representing the previous record value for semiconductor QDs (Table S6, Supporting Information).[2,6a,12b,26]

Cys (0.02 M)-NCs (Figure S13, Supporting Information), onto an ITO substrate. The magnetic tip was magnetized by a permanent magnet with different magnetization directions (field-up or field-down concerning the substrate) for 1 h. Current–voltage (*I*–*V*) curves were measured over 40 times under varying directions of magnetization. The solid traces (**Figure 5a**) represent the average of the *I*–*V* curves, while the shaded traces depict the original data (Figure S14, Supporting Information). Note that the *I*–*V* curves are consistently asymmetric due to the asymmetric potential barriers formed between the NCs and the ITO glass versus the NCs and magnetic tips. The L-Cys-NCs showed a much higher current when the tip was magnetized up than when it was magnetized down, whereas an opposite trend was observed for the D-Cys-NCs. The spin polarization (SP) was calculated as follows:

$$\mathrm{SP} = \frac{I_{\mathrm{up}} - I_{\mathrm{down}}}{I_{\mathrm{up}} + I_{\mathrm{down}}} \times 100\% \quad (2)$$

where I_{up} and I_{down} are the currents measured at a given voltage when the magnetization direction is up and down. The averaged spin polarizations were 83.7 ± 4.4% and −86.5 ± 6.3% for the L-Cys-NCs and D-Cys-NCs, respectively (Figure 5b). which are considerably higher than those reported for previous quantum dots and comparable to the best, intensely studied 2D-perovskite thin films (Figure 5c; Table S6, Supporting Information).[2,6a,12b,26] The strong lattice distortion and the charge transfer between cysteine and the NCs, both of which are expected to contribute to the strong spin polarization effects.[28]

3. Conclusion

We have demonstrated a synthesis route for the chiral $AgBiS_2$ NCs by the direct chiral ligand exchange with L- or D-cysteine chiral ligands. The resulting L- and D-Cys-NC hybrids possess surprisingly strong chirality, with a g-factor of 1×10^{-2} higher than any previously reported chiral ligand-exchanged semiconductor NCs. By experimentally investigating the ligand binding to $AgBiS_2$ NCs and performing related DFT calculations, we find that the bidentate ligand binding mode on the NC surface exerts an unusually strong crystal distortion, while efficient NC-ligand charge transfer between $AgBiS_2$ NCs and cysteine also contributed to the strong CD signal. Furthermore, we have demonstrated a practical application of this material, fabricating the chiral $AgBiS_2$ NC spin filter using our chiral NCs and achieving the highest efficiency among all the reported chiral nanocrystals. Overall, our findings suggested a general route for discovering new strongly chiral nanocrystals among the family of ternary chalcogenides and achieving higher degrees of CD.

4. Experimental Section

Materials: Bismuth (III) acetate ($Bi(OAc)_3$, 99.999%), oleic acid (OA, 90%), hexamethyldisilathiane (HMS, synthesis grade), octadecene (ODE, 90%), toluene (anhydrous, 99.8%), and tetramethylammonium hydroxide pentahydrate (TMAH, 97%) were purchased from Sigma–Aldrich. Silver acetate (AgOAc, 99%) was purchased from J&K Chemical. L(D)-Cysteine (99%) was purchased from Macklin. All the chemicals were purchased and used without further purification.

Synthesis of Pristine OA-NCs: $AgBiS_2$ NCs were synthesized using the previously reported route.[29] In a three-neck round-bottom flask, 1 mmol $Bi(OAc)_3$ and 0.8 mmol Ag(OAc) were dissolved in the mixtures of 6 mL of OA and 4.5 mL of ODE. The temperature was raised to 100 °C under vacuum, and the mixture was degassed overnight. Then, the atmosphere was switched to N_2, and 1 mmol HMS mixed with 0.5 mL of the degassed ODE was swiftly injected into the flask. The heating was stopped, and the mixture was allowed to cool slowly without removing the heating mantel. The NCs were isolated through the addition of 20 mL of acetone and subsequent centrifugation, and re-dispersed in toluene. This purification

process was performed twice, and the NCs were finally dispersed in anhydrous toluene and filtered through a 0.45 µm PTFE filter.

Preparation of Cys-NCs Through the Ligand Exchange: Cys-NCs were synthesized through a solution-phase ligand exchange process, wherein the ligands on the OA-NCs were replaced by L(D)-cysteine. Specifically, L(D)-cysteine (with a different concentration ranging from 0.02 to 0.3 M) and TMAH (with a concentration from 0.2 to 0.5 M) were dissolved in DI water (3 mL). A solution of OA-NCs in toluene (2 θ, 10 mg mL^{-1}) was added to the cysteine solution (3 mL) stirred for 1 h, and stood without stirring until the phases fully separated. The upper toluene layer was carefully removed using a syringe, and the lower aqueous solution was collected and centrifuged at 15 000 rpm for 5 min. The precipitates were collected, redissolved in DI water, and centrifuged again at 2000 rpm for 5 min. The resulting supernatant was retained as the product, while the precipitates were discarded.

Characterization: Ultraviolet–visible (UV–vis) absorption spectra were recorded using a Shimadzu UV3600 spectrometer. The crystalline structure of the $AgBiS_2$ NCs was determined using an X-ray diffractometer (XRD, PW1825 Philips). TEM/HRTEM images and energy-dispersive spectroscopy (EDS) data were obtained on a TEM (JEOL JEM-ARM200F) with an acceleration voltage of 200 kV. Samples were prepared by drop-casting dilute $AgBiS_2$ NCs dispersions onto carbon-coated copper grids. NMR measurements were conducted on a BRUKER AVII 400 NMR instrument. XPS spectra were recorded on a PHI 5600 (Physical Electronics) instrument. Ultraviolet photoelectron spectroscopy (UPS) measurements were conducted on a Kratos Axis Ultra with a base pressure of $\approx 4 \times 10^{-10}$ mbar equipped with a He-I UV-light source (21.22 eV).

CD Measurements: The CD measurements were carried out on a Jasco P-2000 spectropolarimeter with the cuvette placed in the beam path. All spectra obtained were averages of three scans. The CD spectra were recorded from 230 to 600 nm with a 0.5 nm resolution, and the data were presented as the raw CD signal.

mCP-AFM Measurements: The mCP-AFM data were collected on a Dimension Icon AFM system. A Bruker MESP tip, with a length of 226 µm was used in the contact mode, and the Co-Cr-coated tip was subjected to a permanent magnetic field for 1 h and then used for the scan immediately. The *I–V* curves were acquired at least 40 times by ramping the voltage from −1.5 to +1.5 V. To avoid the statistical error caused by the film inhomogeneity, the identical positions on the AFM substrate were measured when changing the tip with opposite directions of magnetic fields. The *I–V* curves were taken at three different points and averaged to ensure accuracy.

Ultrafast Transient Absorption (TA) Spectroscopy: Full-spectral-range transient absorption spectroscopy was carried out using a custom-built pump-probe setup with a Ti: Sapphire regenerative amplifier (Coherent Legend Elite) seeded by a mode-locked Ti:Sapphire oscillator (Coherent Mira 900) as the light source. The 800 nm, 1 kHz output from the amplifier was split into two beams: the primary, more intense beam was directed into an optical parametric amplifier (Coherent Opera Solo) to produce a pump beam with tunable photon energies; the remaining laser power was utilized to generate a supercontinuum probe beam. The probe beam passed through a mechanical translation stage, allowing for a time delay of up to 2 ns between the pump and probe pulses, and was subsequently focused onto a crystal plate. For the Vis-NIR supercontinuum generation (500−1300 nm), a yttrium aluminum garnet (YAG) plate was used, and the fundamental laser line was filtered out by an 800 nm notch filter (Edmund Optics, #86−127) with a 40-nm bandwidth. The differential transmission spectrum of the probe pulse ($\Delta T/T$) was calculated as (($T_{\text{pump ON}} - T_{\text{pump OFF}}$)/$T_{\text{pump OFF}}$). The instrumental response function is 150 fs.

DFT and TD-DFT Calculation Details: Hybrid density functional theory (DFT) calculations used the Coulomb-attenuating method combined with the Becke 3-parameter, Lee, Yang, and Parr hybrid functional (CAM-B3LYP)[13b] for ground state optimizations along with frequency and excitation calculations. The 3–21G basis set for C, S, O, N, and H elements and the LANL2DZ basis set for the Ag and Bi elements were used.[30] The solvation model density (SMD) as a universal continuum solvation model to include solvent effects (H_2O) was used.[31] In addition, the energy levels of the singlet or doublet excitons using time-dependent DFT (TD-DFT) to predict the CD, based on the optimized excited state geometries, were calculated.[32] The DFT-D3 method to include van der Waals attraction (London dispersion) interactions was also applied.[33] All the DFT calculations were performed using Gaussian 16 software, and visualizations were performed using GaussView 6.0.16.[34] The density of states (DOS) and charge transfers were calculated with the Multiwfn 3.8 program.[35]

The lattice distortion (ΔQ) for $AgBiS_2$ NCs after and before the ligand exchange process with cysteine ligands was calculated by the magnitude of the mass-weighted difference in ionic displacements as follows:[36]

$$LD = \sqrt{\sum_{a = \text{Ag, Bi, S}} m_a \Delta R_a^2} \tag{3}$$

where the sum runs over all atoms in the structure, m_a is the atomic mass of Ag (= 107.87 amu), Bi (= 208.98 amu), or S (= 32.06 amu), and ΔR_a is the difference in the ionic configuration (Å) of the atom *a*.

Supporting Information

Supporting Information is available from the Wiley Online Library or from the author.

Acknowledgements

J.E.H. acknowledges funding via IRS22SC117 and DG24SC01, alongside funding from the School of Science and Department of Chemistry at HKUST and from the Research Grants Council of Hong Kong SAR/University Grant Committee (RGC/UGC) via GRF#16306020, as well as the Innovation and Technology Commission (ITC) of Hong Kong via ITS/059/22MX. GHC acknowledges financial support from the General Research Fund (Grant No. 17309620) and Research Grants Council (RGC: T23-713/22-R). GHC acknowledges support from the Hong Kong Quantum AI Lab, AIR@InnoHK of the Hong Kong Government. A. L. R. acknowledges funding from the Research Grants Council of Hong Kong SAR (CityU 11317322), and the Centre for Functional Photonics (CFP) of City University of Hong Kong. L. G. acknowledges funding via the Guangdong Basic and Applied Basic Research Foundation (2024B1515020077) and a high level of special funds (G03034K001).

Conflict of Interest

The authors declare no conflict of interest.

Author Contributions

P.D., D.C., and M.T. contributed equally to this work. P.D. conducted the ligand exchange, the device fabrication, and the characterization unless stated. D.C. synthesized the material, conducted the ligand exchange, and analyzed NMR data. P.D. and D.C. produced the figures and wrote the manuscript. M.T. conducted the DFT calculations and analysis. S.H. conducted CD measurements. M.Q. and B.Z. synthesized the material. M. Q. conducted FTIR, XPS and UPS. P.K.K. conducted mCP-AFM measurements. A.A.S. performed TA spectroscopy measurements. G.C., A.L.R., K.S.W., and L.G. supervised the project and edited the manuscript. J.E.H. supervised the project, analyzed the data, and edited the manuscript.

Data Availability Statement

The data that support the findings of this study are available in the supplementary material of this article.

Keywords

chiral nanocrystals, ligand engineering, metal chalcogenides, spintronics

Received: July 13, 2024
Revised: August 29, 2024
Published online: October 11, 2024

[1] C. Chen, L. Gao, W. Gao, C. Ge, X. Du, Z. Li, Y. Yang, G. Niu, J. Tang, *Nat. Commun.* **2019**, *10*, 1927.
[2] Y.-H. Kim, Y. Zhai, H. Lu, X. Pan, C. Xiao, E. A. Gaulding, S. P. Harvey, J. J. Berry, Z. V. Vardeny, J. M. Luther, M. C. Beard, *Science* **2021**, *371*, 1129.
[3] S. Li, L. Xu, W. Ma, X. Wu, M. Sun, H. Kuang, L. Wang, N. A. Kotov, C. Xu, *J. Am. Chem. Soc.* **2016**, *138*, 306.
[4] A. Chiesa, A. Privitera, E. Macaluso, M. Mannini, R. Bittl, R. Naaman, M. R. Wasielewski, R. Sessoli, S. Carretta, *Adv. Mater.* **2023**, *35*, 2300472.
[5] S.-H. Yang, R. Naaman, Y. Paltiel, S. S. P. Parkin, *Nat. Rev. Phys.* **2021**, *3*, 328.
[6] a) Y.-H. Kim, R. Song, J. Hao, Y. Zhai, L. Yan, T. Moot, A. F. Palmstrom, R. Brunecky, W. You, J. J. Berry, J. L. Blackburn, M. C. Beard, V. Blum, J. M. Luther, *Adv. Funct. Mater.* **2022**, *32*, 2200454; b) G. Li, X. Fei, H. Liu, J. Gao, J. Nie, Y. Wang, Z. Tian, C. He, J.-L. Wang, C. Ji, D. Oron, G. Yang, *ACS Nano* **2020**, *14*, 4196.
[7] a) F. Wu, F. Li, Y. Tian, X. Lv, X. Luan, G. Xu, W. Niu, *Nano Lett.* **2023**, *23*, 8233; b) J. Cai, A.-A. Liu, X.-H. Shi, H. Fu, W. Zhao, L. Xu, H. Kuang, C. Xu, D.-W. Pang, *J. Am. Chem. Soc.* **2023**, *145*, 24375.
[8] A. V. Gonzalez, M. Gonzalez, T. Hanrath, *Sci. Adv. 9*, eadi5520.
[9] Q. Cao, R. Song, C. C. S. Chan, Z. Wang, P. Y. Wong, K. S. Wong, V. Blum, H. Lu, *Adv. Opt. Mater.* **2023**, *11*, 2203125.
[10] X. Gao, X. Zhang, K. Deng, B. Han, L. Zhao, M. Wu, L. Shi, J. Lv, Z. Tang, *J. Am. Chem. Soc.* **2017**, *139*, 8734.
[11] N. Suzuki, Y. Wang, P. Elvati, Z.-B. Qu, K. Kim, S. Jiang, E. Baumeister, J. Lee, B. Yeom, J. H. Bahng, J. Lee, A. Violi, N. A. Kotov, *ACS Nano* **2016**, *10*, 1744.
[12] a) J. Son, S. Ma, Y.-K. Jung, J. Tan, G. Jang, H. Lee, C. U. Lee, J. Lee, S. Moon, W. Jeong, A. Walsh, J. Moon, *Nat. Commun.* **2023**, *14*, 3124; b) H. Lu, J. Wang, C. Xiao, X. Pan, X. Chen, R. Brunecky, J. J. Berry, K. Zhu, M. C. Beard, Z. V. Vardeny, *Sci. Adv. 5*, eaay0571.
[13] a) V. A. Kuznetsova, E. Mates-Torres, N. Prochukhan, M. Marcastel, F. Purcell-Milton, J. O'Brien, A. K. Visheratina, M. Martinez-Carmona, Y. Gromova, M. Garcia-Melchor, Y. K. Gun'ko, *ACS Nano* **2019**, *13*, 13560; b) J. K. Choi, B. E. Haynie, U. Tohgha, L. Pap, K. W. Elliott, B. M. Leonard, S. V. Dzyuba, K. Varga, J. Kubelka, M. Balaz, *ACS Nano* **2016**, *10*, 3809.
[14] D. Chen, P. K. Ko, C. H. A. Li, B. Zou, P. Geng, L. Guo, J. E. Halpert, *ACS Energy Lett.* **2023**, *8*, 410.
[15] Z. N. Georgieva, B. P. Bloom, S. Ghosh, D. H. Waldeck, *Adv. Mater.* **2018**, *30*, 1800097.
[16] a) Y. Wang, S. R. Kavanagh, I. Burgués-Ceballos, A. Walsh, D. O. Scanlon, G. Konstantatos, *Nat. Photonics* **2022**, *16*, 235; b) M. Righetto, Y. Wang, K. A. Elmestekawy, C. Q. Xia, M. B. Johnston, G. Konstantatos, L. M. Herz, *Adv. Mater.* **2023**, *35*, 2305009.
[17] Y.-T. Huang, S. R. Kavanagh, M. Righetto, M. Rusu, I. Levine, T. Unold, S. J. Zelewski, A. J. Sneyd, K. Zhang, L. Dai, A. J. Britton, J. Ye, J. Julin, M. Napari, Z. Zhang, J. Xiao, M. Laitinen, L. Torrente-Murciano, S. D. Stranks, A. Rao, L. M. Herz, D. O. Scanlon, A. Walsh, R. L. Z. Hoye, *Nat. Commun.* **2022**, *13*, 4960.
[18] a) S. Akhil, R. G. Balakrishna, *J. Mater. Chem. A* **2022**, *10*, 8615; b) M. Bernechea, N. Cates, G. Xercavins, D. So, A. Stavrinadis, G. Konstantatos, *Nat. Photonics* **2016**, *10*, 521; c) P. Geng, D. Chen, S. B. Shivarudraiah, X. Chen, L. Guo, J. E. Halpert, *Adv. Sci.* **2023**, *10*, 2300177.
[19] a) X. Shao, Y. Wu, S. Jiang, B. Li, T. Zhang, Y. Yan, *J. Mater. Chem. C* **2021**, *9*, 555; b) M. Puri, V. E. Ferry, *ACS Nano* **2017**, *11*, 12240; c) Y. Wu, T. Zhao, X. Shao, J. Chen, T. Zhang, B. Li, S. Jiang, *Small* **2023**, *19*, 2301034.
[20] T. Kurihara, Y. Noda, K. Takegoshi, *ACS Omega* **2019**, *4*, 3476.
[21] E. Awoonor-Williams, C. N. Rowley, *J. Chem. Theory Comput.* **2016**, *12*, 4662.
[22] F. Jalilehvand, N. S. Sisombath, A. C. Schell, G. A. Facey, *Inorg. Chem.* **2015**, *54*, 2160.
[23] J. Yeom, B. Yeom, H. Chan, K. W. Smith, S. Dominguez-Medina, J. H. Bahng, G. Zhao, W.-S. Chang, S.-J. Chang, A. Chuvilin, D. Melnikau, A. L. Rogach, P. Zhang, S. Link, P. Král, N. A. Kotov, *Nat. Mater.* **2015**, *14*, 66.
[24] A. Lang, A. Brif, I. Polishchuk, A. N. Fitch, J. Feldmann, B. Pokroy, *Adv. Opt. Mater.* **2022**, *10*, 2200203.
[25] a) J. Bardeen, W. Shockley, *Phys. Rev.* **1950**, *80*, 72; b) P. Ding, Y. Zhu, Z. Han, L. Li, L. Zhang, Y. Cai, D. J. Singh, L. Zhang, W. Zhang, S. Shin, J. Yang, W. Liu, L. Guo, *Phys. Rev. B* **2023**, *108*, 064310.
[26] a) G. Bullard, F. Tassinari, C.-H. Ko, A. K. Mondal, R. Wang, S. Mishra, R. Naaman, M. J. Therien, *J. Am. Chem. Soc.* **2019**, *141*, 14707; b) B. P. Bloom, V. Kiran, V. Varade, R. Naaman, D. H. Waldeck, *Nano Lett.* **2016**, *16*, 4583; c) Y. Lu, Q. Wang, R. Chen, L. Qiao, F. Zhou, X. Yang, D. Wang, H. Cao, W. He, F. Pan, Z. Yang, C. Song, *Adv. Funct. Mater.* **2021**, *31*, 2104605; d) S. Mishra, E. G. Bowes, S. Majumder, J. A. Hollingsworth, H. Htoon, A. C. Jones, *ACS Nano* **2024**, *18*, 8663.
[27] a) B. P. Bloom, Y. Paltiel, R. Naaman, D. H. Waldeck, *Chem. Rev.* **2024**, *124*, 1950; b) F. Pop, N. Zigon, N. Avarvari, *Chem. Rev.* **2019**, *119*, 8435.
[28] B. P. Bloom, B. M. Graff, S. Ghosh, D. N. Beratan, D. H. Waldeck, *J. Am. Chem. Soc.* **2017**, *139*, 9038.
[29] D. Chen, S. B. Shivarudraiah, P. Geng, M. Ng, C. H. A. Li, N. Tewari, X. Zou, K. S. Wong, L. Guo, J. E. Halpert, *ACS Appl. Mater. Interfaces* **2022**, *14*, 1634.
[30] a) M. J. Hülsey, B. Zhang, Z. Ma, H. Asakura, D. A. Do, W. Chen, T. Tanaka, P. Zhang, Z. Wu, N. Yan, *Nat. Commun.* **2019**, *10*, 1330; b) G. Xu, C. Li, C. Chi, L. Wu, Y. Sun, J. Zhao, X.-H. Xia, S. Gou, *Nat. Commun.* **2022**, *13*, 3064.
[31] A. V. Marenich, C. J. Cramer, D. G. Truhlar, *J. Phys. Chem. B* **2009**, *113*, 6378.
[32] M. Tamtaji, S. Cai, W. Wu, T. Liu, Z. Li, H.-Y. Chang, P. R. Galligan, S.-I. Iida, X. Li, F. Rehman, K. Amine, W. A. Goddard, Z. Luo, *J. Mater. Chem. A* **2023**, *11*, 7513.
[33] a) L. Zhou, J. M. P. Martirez, J. Finzel, C. Zhang, D. F. Swearer, S. Tian, H. Robatjazi, M. Lou, L. Dong, L. Henderson, P. Christopher, E. A. Carter, P. Nordlander, N. J. Halas, *Nat. Energy* **2020**, *5*, 61; b) M. Tamtaji, Q. Peng, T. Liu, X. Zhao, Z. Xu, P. R. Galligan, M. D. Hossain, Z. Liu, H. Wong, H. Liu, K. Amine, Y. Zhu, W. A. Goddard Iii, W. Wu, Z. Luo, *Nano Energy* **2023**, *108*, 108218.
[34] H. M. Badran, K. M. Eid, H. Y. Ammar, *Results Phys.* **2021**, *23*, 103964.
[35] T. Lu, F. Chen, *J. Comput. Chem.* **2012**, *33*, 580.
[36] C. Linderälv, W. Wieczorek, P. Erhart, *Phys. Rev. B* **2021**, *103*, 115421.
[37] B. Zou, D. Chen, M. Qammar, P. Ding, P. K. Ko, W. Wu, S. B. Shivarudraiah, H. Yan, J. E. Halpert, ACS Appl. Energy Mater **2024**, https://doi.org/10.1021/acsaem.4c01307.